# $Bi_{1-x}Sb_x$ Alloy Nanocrystals: Colloidal Synthesis, Charge Transport, and Thermoelectric Properties

**Hao Zhang,[†] Jae Sung Son,[†] Jaeyoung Jang,[†] Jong-Soo Lee,[†] Wee-Liat Ong,[⊥] Jonathan A. Malen,[§,⊥] and Dmitri V. Talapin[†,‡,*]**

[†]Department of Chemistry and James Frank Institute, University of Chicago, Chicago, Illinois 60637, United States, [‡]Center for Nanoscale Materials, Argonne National Laboratory, Argonne, Illinois 60439, United States, [§]Department of Materials Science and Engineering, Carnegie Mellon University, Pittsburgh, Pennsylvania 15213, United States, and [⊥]Department of Mechanical Engineering, Carnegie Mellon University, Pittsburgh, Pennsylvania 15213, United States

**ABSTRACT** Nanostructured $Bi_{1-x}Sb_x$ alloys constitute a convenient system to study charge transport in a nanostructured narrow-gap semiconductor with promising thermoelectric properties. In this work, we developed the colloidal synthesis of monodisperse sub-10 nm $Bi_{1-x}Sb_x$ alloy nanocrystals (NCs) with controllable size and compositions. The surface chemistry of $Bi_{1-x}Sb_x$ NCs was tailored with inorganic ligands to improve the interparticle charge transport as well as to control the carrier concentration. Temperature-dependent (10−300 K) electrical measurements were performed on the $Bi_{1-x}Sb_x$ NC based pellets to investigate the effect of surface chemistry and grain size (~10−40 nm) on their charge transport properties. The Hall effect measurements revealed that the temperature dependence of carrier mobility and concentration strongly depended on the grain size and the surface chemistry, which was different from the reported bulk behavior. At low temperatures, electron mobility in nanostructured $Bi_{1-x}Sb_x$ was directly proportional to the average grain size, while the concentration of free carriers was inversely proportional to the grain size. We propose a model explaining such behavior. Preliminary measurements of thermoelectric properties showed a ZT value comparable to those of bulk $Bi_{1-x}Sb_x$ alloys at 300 K, suggesting a potential of $Bi_{1-x}Sb_x$ NCs for low-temperature thermoelectric applications.

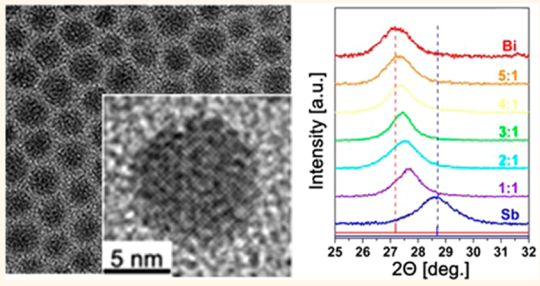


**KEYWORDS:** $Bi_{1-x}Sb_x$ nanocrystals · electrical conductivity · Hall effect measurements · grain boundaries · surface chemistry · thermoelectrics

Bismuth antimony alloys ($Bi_{1-x}Sb_x$, $0 < x < 1$) have attracted extensive attention due to their peculiar physical properties[1,2] and potential applications as the best n-type thermoelectric material at very low temperatures (20−200 K).[3−5] $Bi_{1-x}Sb_x$ was also one of the first materials revealing the topological insulator behavior.[6,7] The band structure (Figure 1A) and related electronic properties of $Bi_{1-x}Sb_x$ alloys are strongly dependent on the content of antimony ($x$).[1,5] For $x < 0.07$ and $x > 0.22$, there is an overlap between the valence band (T or H band) and the conduction band (L band), leading to the semimetallic (SM) behavior resembling that of Bi and Sb. In the range $0.07 < x < 0.22$, $Bi_{1-x}Sb_x$ alloys show semiconductor (SC) properties with a maximum band gap of ~25−30 meV,[1,5] high carrier mobility, small effective mass ($m_e^*$ can be as small as $0.002m_e^0$ in bulk $Bi_{1-x}Sb_x$ alloys,[8,9] where $m_e^0$ is the free electron mass), and highly nonparabolic energy momentum dispersion relation in the L valley.[1,10] As a result, a large Bohr radius (>30 nm[1,10−13]) for electrons was predicted for the Bi-rich $Bi_{1-x}Sb_x$ alloys, which could induce strong quantum confinement in low-dimensional $Bi_{1-x}Sb_x$ nanostructures and contribute to the band rearrangement in the predicted semimetal-to-semiconductor transition[13,14] and the disappearance of the direct band gap phase[14] ($0.09 < x < 0.17$ in bulk).

The material dimensionality and size have a strong influence on the transport properties of $Bi_{1-x}Sb_x$ alloys. Dresselhaus *et al.* predicted that the thermoelectric figure of merit ($ZT = (S^2\sigma/\kappa)T$, where $S$ is the Seebeck coefficient, also known as thermopower, $\sigma$ is the electrical conductivity, and $\kappa$ is the thermal conductivity) can approach ~2.5 at

* Address correspondence to dvtalapin@uchicago.edu.

Received for review September 6, 2013 and accepted October 17, 2013.

**Published online October 17, 2013**
**10.1021/nn404692s**

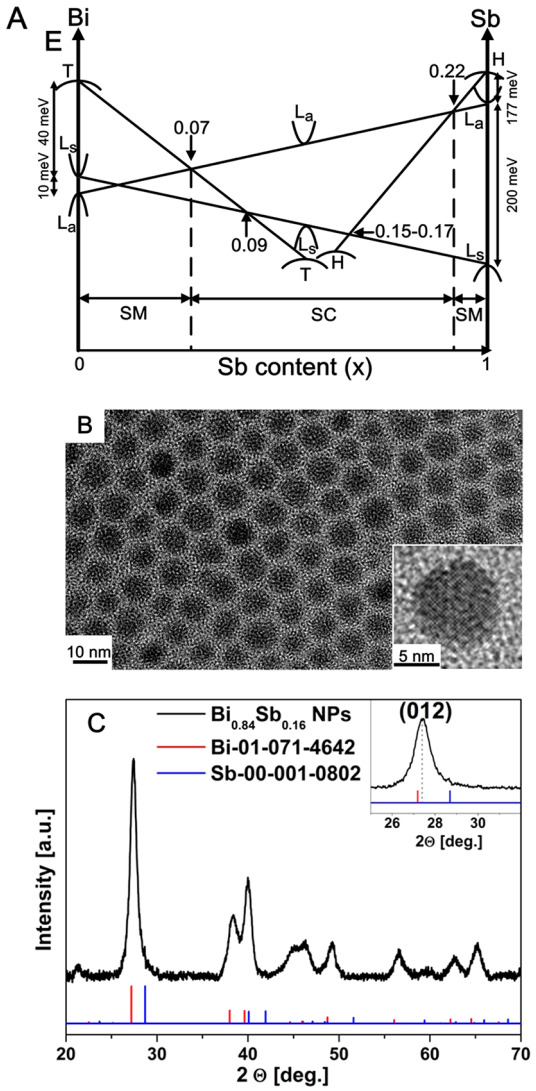


**Figure 1. (A) Schematic band diagram of bulk $Bi_{1-x}Sb_x$ alloys as a function of Sb content ($x$) near 0 K;[1,5] (B) TEM and (C) XRD pattern of 8.8 nm $Bi_{0.84}Sb_{0.16}$ NCs. Inset in (B) shows the HRTEM of $Bi_{0.84}Sb_{0.16}$ NCs. The vertical lines in (C) show the corresponding positions and intensities of X-ray reflections for bulk Bi and Sb. Inset in (C) shows the magnified (012) reflection, demonstrating the shift of diffraction for $Bi_{0.84}Sb_{0.16}$ NCs compared to pure Bi and Sb.**

77 K for $Bi_{1-x}Sb_x$ nanowires with a diameter smaller than 20 nm.[14] Such unprecedentedly high ZT was attributed to the increase in the density of states close to the Fermi level of $Bi_{1-x}Sb_x$ nanowires due to the quantum confinement. So far, most experimental charge transport studies have been performed on polycrystalline $Bi_{1-x}Sb_x$ alloys[15−19] with grain size in the range of 100 nm to hundreds of micrometers and on $Bi_{1-x}Sb_x$ nanowires[10,13] with >∼40 nm diameter, respectively. To the best of our knowledge, transport and thermoelectric properties of $Bi_{1-x}Sb_x$ alloys with grain sizes below ∼40 nm have not yet been studied because of the lack of uniform, high-quality $Bi_{1-x}Sb_x$ nanostructures, especially $Bi_{1-x}Sb_x$ NCs smaller than 20 nm. In view of their peculiar physical properties and promising thermoelectric performance, it is highly desirable to develop a method for synthesizing sub-10 nm $Bi_{1-x}Sb_x$ NCs with good size distribution and precise compositional control. However, it still remains a challenge mainly due to the lack of appropriate precursors. Until now, there have been only a few attempts on the synthesis of $Bi_{1-x}Sb_x$ nanoparticles (NPs).[20−22] Previously synthesized $Bi_{1-x}Sb_x$ NPs suffered from poor morphological control with a broad size distribution, which hampered the study of their size-dependent physical properties. In addition, these NPs were insoluble, which hindered their use in solution-processed thin-film devices.

In this work, we report the first colloidal synthesis of uniform sub-10 nm compositionally homogeneous $Bi_{1-x}Sb_x$ alloy NCs, where the composition and particle size can be tuned by adjusting the reaction parameters. We demonstrate that the surface chemistry of $Bi_{1-x}Sb_x$ NCs can be tailored by exchange of organic ligands with metal-free chalcogenides ($S^{2-}$, $Se^{2-}$, $Te^{2-}$)[23] or metal chalcogenide complexes (MCC) ligands[24,25] ($K_4SnTe_4$, *etc.*). These approaches offer the possibility of tuning the electrical properties of the NCs by introducing doping[26,27] from ligands and reducing interparticle distance.[28−30] More importantly, these sub-10 nm $Bi_{1-x}Sb_x$ NCs could constitute a good model system for the charge transport studies in $Bi_{1-x}Sb_x$ alloys with tunable grain sizes; they also represent an example of a nanostructured semiconductor with very narrow band gap. Temperature-dependent conductivity and Hall effect measurements revealed that the charge transport behavior of the $Bi_{1-x}Sb_x$ NC pellets is dominated by interfacial carrier scattering, which is different from that of bulk $Bi_{1-x}Sb_x$, while carrier concentration is directly related to the interface-to-volume ratio. The effect of surface chemistry on charge transport properties of the $Bi_{1-x}Sb_x$ NC based pellets was also investigated. Finally, thermoelectric properties of the $Bi_{1-x}Sb_x$ NC based pellets were measured, and a ZT of ∼0.23 was obtained at 300 K without systematic optimizations, which is comparable to those for $Bi_{1-x}Sb_x$ single crystals and polycrystalline $Bi_{1-x}Sb_x$ alloys.

## RESULTS AND DISCUSSIONS

**Colloidal Synthesis of $Bi_{1-x}Sb_x$ NCs.** $Bi_{1-x}Sb_x$ NCs were synthesized by the injection of bismuth(III)tris[bis-(trimethylsilyl)amide] ($Bi[N(SiMe_3)_2]_3$) and tris(dimethylamido) antimony(III) ($Sb(NMe_2)_3$) into hot oleylamine (OLA) in the presence of a strong reducing agent, lithium triethylborohydride ($LiEt_3BH$, also known as superhydride). The choice of $Bi[N(SiMe_3)_2]_3$ was based on the previous success in the synthesis of Bi NCs.[31,32] $Sb(NMe_2)_3$ is a widely used precursor for organometallic vapor phase epitaxial (OMVPE) growth of III−V compounds.[33,34] The addition of $LiEt_3BH$ was imperative for the formation of homogeneous $Bi_{1-x}Sb_x$ alloy NCs in

view of the large discrepancy in the reactivity of the two precursors in oleylamine. In the absence of $LiEt_3BH$, the synthesis resulted in the formation of pure Bi, regardless of the ratio between $Bi[N(SiMe_3)_2]_3$ and $Sb(NMe_2)_3$ and other reaction parameters. Similar to the case in a recently reported InSb NC synthesis,[35] we propose that $LiEt_3BH$ rapidly reduced the trivalent $Bi[N(SiMe_3)_2]_3$ and $Sb(NMe_2)_3$ to the highly reactive $Bi^{(0)}$ and $Sb^{(0)}$ intermediates, which subsequently underwent the nucleation and growth processes and finally formed the homogeneous alloys. The addition of $Li[N(SiMe_3)_2]$ was essential to achieve a narrow size distribution and perfectly spherical NCs, since the $N(SiMe_3)_2$ group may coordinate the surface metal atoms during the growth of NCs.[31,36]

Figure 1B shows a typical transmission electron microscopy (TEM) image of the $Bi_{1-x}Sb_x$ ($Bi_{0.84}Sb_{0.16}$, confirmed by inductively coupled plasma optical emission spectroscopy (ICP-OES) analysis) NCs with an average size of 8.8 nm. The NCs have uniform, nearly spherical shapes. The size distribution of the NCs was ~10% without size-selective steps, which is a significant improvement compared to all previous reports on the $Bi_{1-x}Sb_x$ synthesis.[20−22] The high-resolution TEM (HRTEM) image (Figure 1B, inset) reveals high crystallinity of the NCs, and the *d*-spacing of the lattice fringes (0.32−0.33 nm) is in accordance with the lattice parameter of the Bi-rich $Bi_{1-x}Sb_x$ alloy.[31] The powder X-ray diffraction (XRD) pattern of $Bi_{1-x}Sb_x$ NCs in Figure 1C shows reflections shifted to higher $2\theta$ angles from those of pure bulk Bi with a rhombohedral crystal structure ($R\bar{3}m$), as a result of the replacement of Bi atoms by the smaller Sb atoms. It is noteworthy that no secondary peaks were detected, indicating the formation of homogeneous $Bi_{1-x}Sb_x$ alloys. In general, it is known to be difficult to prepare homogeneous $Bi_{1-x}Sb_x$ alloys by solid-state synthesis because of the strong tendency for phase segregation.[37] The size of NCs calculated from the width of diffraction peaks by Scherrer's equation was in accordance with that estimated in the TEM images, suggesting the size uniformity and high crystallinity of the NCs.

The average size of $Bi_{1-x}Sb_x$ NCs can be tuned by adjusting the reaction time and temperature. As the reaction time increased from 15 s to 2 min, the average size slightly increased from <9 nm to 11 nm, as shown in Figure S1A−C. We found that the Sb content was almost independent of the reaction time (Table S1). On the other hand, higher injection temperature led to a significant increase in the particle size. $Bi_{1-x}Sb_x$ NCs with sizes ranging from ~7 to ~16 nm were obtained by elevating the injection temperature from 60 °C to 90 °C, as shown in Figure S2A−C. The narrowing in the diffraction peaks also indicated the increase in particle size with higher injection temperatures, as shown in Figure S2D. The Sb content was also maintained in the range from 0.15 to 0.17, regardless of the reaction

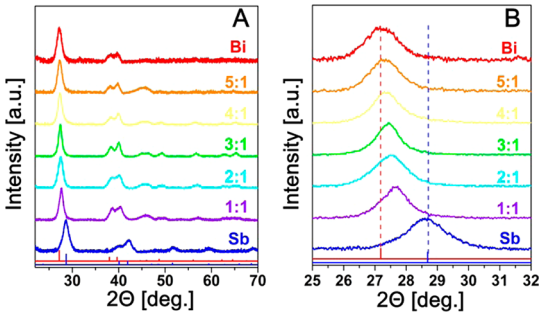


**Figure 2. (A) XRD patterns of $Bi_{1-x}Sb_x$ NCs with different Bi-to-Sb ratios. (B) Magnified (012) region showing progressive shift with increasing Sb content from pure Bi to pure Sb NCs. The vertical lines show the corresponding positions and intensities of X-ray reflections for bulk Bi (red) and Sb (blue).**

**TABLE 1. ICP-OES Analysis of $Bi_{1-x}Sb_x$ NCs with Various Sb Contents**

| Bi-to-Sb ratio | Sb content (*x*) |
|---|---|
| $Bi[N(SiMe_3)_2]_3$ | 0.00 |
| 5:1 | 0.11 |
| 4:1 | 0.16 |
| 3:1 | 0.19 |
| 2:1 | 0.25 |
| 1:1 | 0.42 |
| $Sb(NMe_2)_3$ | 1.00 |

temperatures. Such a small change in Sb content could be attributed to the balanced reactivities of $Bi[N(SiMe_3)_2]_3$ and $Sb(NMe_2)_3$ in the presence of $LiEt_3BH$, which allowed a fine control of the average particle size with maintained Sb contents by varying the reaction time and injection temperature.

More importantly, we could synthesize uniform $Bi_{1-x}Sb_x$ NCs with various Sb contents by simply adjusting the ratio between $Bi[N(SiMe_3)_2]_3$ and $Sb(NMe_2)_3$ (Bi-to-Sb ratio) in the precursor solution (Figure S3). Sb contents were readily tuned from $x \approx 0$ (pure Bi) to $x \approx 1$ (pure Sb). As shown in the XRD patterns in Figure 2, the diffraction peaks progressively shifted to higher $2\theta$ angles with increasing Sb content (*i*.e., decreasing Bi-to-Sb ratio). The Sb content determined by ICP-OES analysis (Table 1) was slightly lower compared to the Sb ratio in the precursor solution. The lower Sb content reflected slightly lower reactivity of $Sb(NMe_2)_3$ in oleylamine compared to that of $Bi[N(SiMe_3)_2]_3$, as discussed above. On the basis of the XRD patterns, the lattice constants *a* and *c* of various $Bi_{1-x}Sb_x$ NCs were calculated using the hexagonal cell structure.[38] As expected, pure Bi and Sb NCs exhibited similar lattice parameters with the bulk counterparts. The decrease in *a* and *c* was linear with increasing Sb content, in agreement with Vegard's law,[39] as shown in Figure S3E and F.

The synthesis could also be readily scaled up to the subgram scale without notable changes in the uniformity and homogeneity of the $Bi_{1-x}Sb_x$ NCs (Figure S4). The XRD pattern showed distinct features of a $Bi_{1-x}Sb_x$

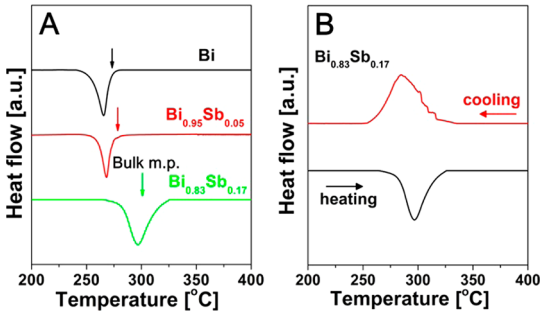


**Figure 3. (A) DSC curves for Bi, $Bi_{0.95}Sb_{0.05}$, and $Bi_{0.83}Sb_{0.17}$ NCs obtained by a large-scale synthesis. The data are shifted vertically for clarity. The arrows indicate the melting points for corresponding bulk Bi and $Bi_{1-x}Sb_x$ alloys. (B) DSC heating and cooling curves for $Bi_{0.83}Sb_{0.17}$ NCs.**

alloy, and the Sb content was confirmed as $x \approx 0.17$ by ICP-OES analysis. In the large batch synthesis, ~0.7–0.8 g of $Bi_{1-x}Sb_x$ NCs was obtained with a chemical yield of >80%. The large-scale synthesis of uniform, homogeneous $Bi_{1-x}Sb_x$ alloy NCs facilitated the experimental studies on their charge transport and thermoelectric properties, as discussed in the following sections.

To further confirm the homogeneity of the synthesized $Bi_{1-x}Sb_x$ NCs, we carried out differential scanning calorimetry (DSC) studies for three representative samples (Bi, $Bi_{0.95}Sb_{0.05}$, $Bi_{0.83}Sb_{0.17}$). Figure 3A shows that all three thermograms exhibit only one endothermic peak corresponding to the melting behavior without any other features, indicating the high homogeneity of the synthesized alloy NCs. The shift in the melting point (estimated by the onset of endothermic peak) toward higher temperatures with increasing Sb content was attributed to the higher melting point of Sb (~671 °C) compared to Bi (~273 °C), in line with previous reports on bulk[40] or nanostructured[20] $Bi_{1-x}Sb_x$ alloys. In addition, no peaks were observed in the high-temperature range (400–600 °C) of the DSC curves for NCs (*e.g.*, $Bi_{0.83}Sb_{0.17}$ NCs, Figure S5), indicating the absence of impurites with high Sb contents. Generally, phase segregation is a well-known problem that occurs in bulk $Bi_{1-x}Sb_x$ alloys.[37] It originates from the large discrepancy between the liquidus and solidus lines in the Bi–Sb binary phase diagram.[37] As an example, for polycrystalline $Bi_{1-x}Sb_x$ prepared by ball milling, a second endothermic peak was observed at higher temperatures in the thermograms due to the coexistence of alloys with richer Sb contents.[40] Similar phase segregation was observed in our $Bi_{1-x}Sb_x$ NC samples during cooling from the melt (*e.g.*, $Bi_{0.83}Sb_{0.17}$ NCs, reverse scan in Figure 3B), indicated by the presence of several peaks with higher melting points than the main phase. Moreover, all of the $Bi_{1-x}Sb_x$ NCs (~9 nm) showed suppression of the melting point by about 20 °C compared to those of the corresponding bulk alloys (indicated by arrows in Figure 3A), which is in agreement with previous reports on the size-dependent melting point of Bi NPs.[41]

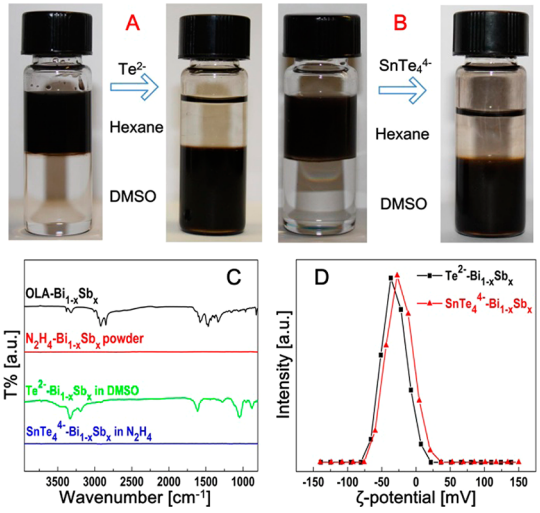


**Figure 4. (A and B) Photographs of the transfer of $Bi_{1-x}Sb_x$ NCs from hexane to DMSO upon the exchange of original OLA ligands with $Te^{2-}$ and $SnTe_4^{4-}$, respectively. (C) FTIR of $Bi_{1-x}Sb_x$ NCs with OLA, after $N_2H_4$ treatment, and with inorganic ligands. (D) ζ-Potential distribution of $Bi_{1-x}Sb_x$ NCs capped with $Te^{2-}$ and $SnTe_4^{4-}$, respectively, in DMSO.**

**Surface Chemistry of $Bi_{1-x}Sb_x$ NCs.** We also explored the surface chemistry of the $Bi_{1-x}Sb_x$ NCs. The long-chain organic capping ligands used for NC synthesis represent a major bottleneck for charge transport in NC assemblies.[24,28,29] Previous reports have demonstrated the use of small inorganic molecules, including $N_2H_4$,[28] molecular metal chalcogenide complexes,[24,25] and metal-free chalcogenides,[23] to remove or replace the long-chain organic ligands for colloidal NCs and facilitate electronic[27,30] and thermal transport[42] in layers of close-packed NCs. In addition, the inorganic ligands can induce remote doping to the NCs' core, providing the opportunity for the fine control of electrical properties for NC-based electronic devices.[26] For this purpose, $N_2H_4$ treatment was carried out on the $Bi_{1-x}Sb_x$ NCs to remove the residual OLA ligands. Moreover, we checked the feasibility of the phase transfer of OLA-capped $Bi_{1-x}Sb_x$ NCs from a nonpolar solvent (hexane) into a polar solvent containing inorganic ligands ($K_2S$ or $Na_2X$ (X = S, Se, or Te) or MCC ($K_4SnTe_4$, $(N_2H_5)_4Sn_2S_6$, $(N_2H_5)_4Sn_2Se_6$, *etc.*)). As a solvent for inorganically capped NCs, we used aprotic dimethylsulfoxide (DMSO) with a moderate polarity ($\varepsilon \approx 47$). This solvent worked better than protic polar solvents such as $N_2H_4$, formamide (FA), or *N*-methyl formamide (NMF), presumably because of the presence of trace amounts of residual superhydride in the $Bi_{1-x}Sb_x$ NCs solutions.

Upon gentle shaking or stirring (from <1 min to several hours, depending on the ligand), we observed a complete phase transfer of NCs from nonpolar to polar solvent containing inorganic ligands (Figure 4A and B). After purification, the inorganically capped $Bi_{1-x}Sb_x$ NCs could be redispersed in various polar solvents such as DMSO, NMF, FA, and $N_2H_4$. The complete removal of original organic ligands was confirmed by Fourier

transform infrared (FTIR) analysis, as shown in Figure 4C, where the strong bands for C−H stretching in OLA almost disappeared. The absorption bands for $Te^{2-}$-capped $Bi_{1-x}Sb_x$ NCs can be attributed to the presence of DMSO solvent. On the other hand, the $SnTe_4^{2-}$-capped $Bi_{1-x}Sb_x$ NCs dispersed in a more volatile $N_2H_4$ solvent exhibited a featureless FTIR spectrum. The inorganically capped $Bi_{1-x}Sb_x$ NCs showed excellent long-term colloidal stability, which was achieved by binding the negatively charged anions on the NC surface, as indicated by a negative $\zeta$-potential (∼−35 and −24 mV for $Te^{2-}$- and $SnTe_4^{4-}$-capped $Bi_{1-x}Sb_x$ NCs, respectively, Figure 4D). In addition, negligible changes were observed in the morphology and crystalline features of $Bi_{1-x}Sb_x$ NCs after ligand exchange (Figure S6). Among the inorganic ligand capped $Bi_{1-x}Sb_x$ NCs, the $Te^{2-}$-capped NCs are of particular interest in view of the fact that Te is considered an effective n-type dopant[43] for $Bi_{1-x}Sb_x$ alloys, and the $Te^{2-}$ ligand could induce remote doping to the $Bi_{1-x}Sb_x$ NCs.

**Charge Transport Properties of $Bi_{1-x}Sb_x$ NC Based Pellets.** To study the charge transport behavior of $Bi_{1-x}Sb_x$ NC assemblies, we prepared square- or disk-shaped pellets (inset in Figure 5A) by pressing $Bi_{1-x}Sb_x$ NC powder at room temperature. The powdery form of $Bi_{1-x}Sb_x$ NCs was prepared following the procedure described in the Experimental Section. The $Bi_{1-x}Sb_x$ NCs maintained their initial sizes (<10 nm) in the powdery form, as shown in the TEM image (Figure S7). $Bi_{1-x}Sb_x$ NCs with an Sb content of $x \approx 0.17$ were used, which was within the range of the Sb contents for the maximum band gap and optimal thermoelectric performance as reported for bulk $Bi_{1-x}Sb_x$[5] and $Bi_{1-x}Sb_x$ nanowires.[14]

To investigate the effect of surface chemistry (*i.e.*, surfactants and ligands) on the charge transport through strongly electronically coupled $Bi_{1-x}Sb_x$ nanograins, original organic surfactants were removed using $N_2H_4$ treatment or ligand exchange with $Te^{2-}$ prior to pellet formation. After pressing, a small grain growth (∼10 to ∼15 nm for NC powder without $N_2H_4$ treatment) was detected by XRD using Scherrer's equation. We attributed it to minor NC sintering under pressure. The grain growth of NC-based pellets could be further controlled by thermal annealing under an inert atmosphere and monitored by the widths of XRD peaks (Figure S8). After annealing at 250 °C for ∼30 min, the calculated average grain size in $Bi_{0.83}Sb_{0.17}$ NC based pellets increased from ∼15 to ∼35 nm (OLA-capped) and from ∼18 nm to ∼40 nm ($N_2H_4$-treated). It should be noted that the grain size still remained below 50 nm, and no peaks for secondary phase or other impurities were detected after annealing. In the following discussion, we will mainly focus on five types of pellets: as-pressed OLA-capped NCs (**I**); as-pressed $N_2H_4$-treated NCs (**II**); OLA-capped NCs annealed at 250 °C for 30 min (**III**); $N_2H_4$-treated NCs annealed at 250 °C for 30 min (**IV**); and as-pressed $Te^{2-}$-capped NCs (**V**). The comparative study of this series of pellets allowed us to reveal the effects of grain size and surface ligands on electronic transport in nanocrystalline $Bi_{1-x}Sb_x$ alloys.

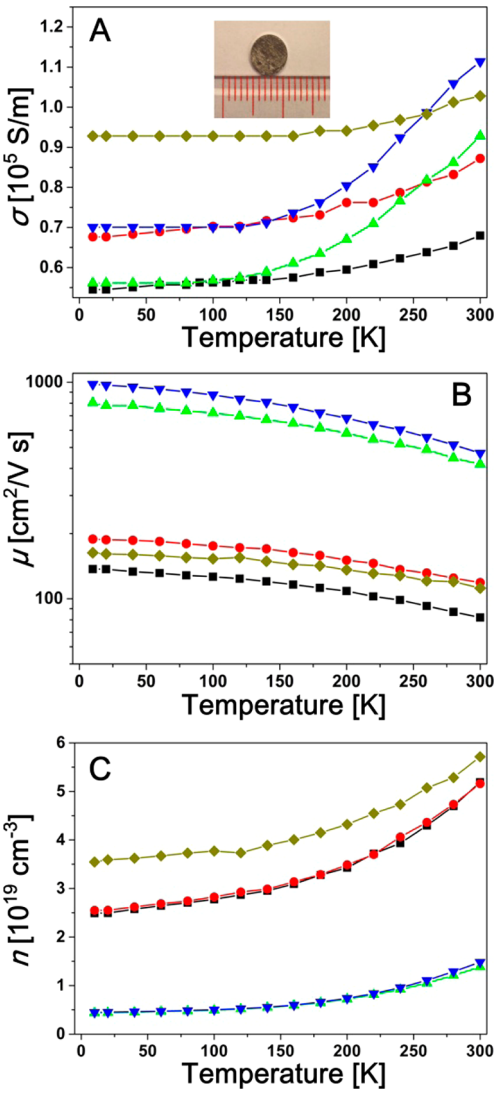


**Figure 5. Temperature dependence of electrical conductivity (A), carrier mobility (B), and carrier concentration (C) of various $Bi_{0.83}Sb_{0.17}$ NC based pellets, pellet I (as-pressed, OLA, black square), pellet II (as-pressed, $N_2H_4$, red circle), pellet III (250 °C annealed, OLA, green upward triangle), pellet IV (250 °C annealed, $N_2H_4$, blue downward triangle), and pellet V (as-pressed, $Te^{2-}$, dark yellow diamond). Inset in (A): Photograph of a disk-shaped $Bi_{0.83}Sb_{0.17}$ NC based pellet ($N_2H_4$-treated, annealed at 250 °C for 30 min, diameter 6 mm, thickness 1 mm).**

**Temperature-Dependent Electrical Conductivity.** The temperature dependence of electrical conductivities ($\sigma$) of the $Bi_{0.83}Sb_{0.17}$ NC based pellets was measured at temperatures from 300 to 10 K (Figure 5A). At room temperature, all samples exhibited $\sigma$ in the range $10^4$–$10^5$ S/m. For reference, the reported values of bulk $Bi_{1-x}Sb_x$ alloys are in the range $2 \times 10^5$ to $5 \times 10^5$ S/m.[4,5,16,44] The room-temperature (300 K) $\sigma$ generally increased with

the average grain size in the NC samples (Figure S9). Such an increase of $\sigma$ can be attributed to the lower density of grain boundaries as well as the elimination of voids during grain growth. However, below ~140–160 K, the as-pressed and annealed pellets showed almost the same $\sigma$ (**I** and **III**, **II** and **IV**, respectively), despite the significant difference in their average grain sizes. This unexpected feature will be discussed in the following section.

As temperature decreased from 300 K to ~140–160 K, all samples showed a monotonic decrease in $\sigma$, which is similar to the reported behavior of semiconducting $Bi_{1-x}Sb_x$[13] and Bi[45] nanowires. On the contrary, it has been reported that semimetallic Bi nanowires (>50 nm in diameter) exhibit a non-monotonic temperature dependence of resistance.[4,5,19,45] Below ~140–160 K, a temperature-independent conductivity was observed in all the samples, which appears to result from a compensation effect where the mobility increase at low temperature is accompanied by a decrease of the free carrier concentration. Interestingly, all as-pressed samples (**I**, **II**, and **V**) with small grains showed weaker temperature dependence compared to the annealed pellets. This can be explained by the dominance of carrier scattering at the interfaces between the NCs, which is expected to be nearly temperature independent compared to other scattering mechanisms. Further details will be discussed in the following section.

Surface chemistry of NCs also imposed a strong influence on $\sigma$ of the pellets. The samples treated by $N_2H_4$ showed higher electrical conductivities (Figure 5A and Figure S9), probably due to the effective removal of insulating organic residues from the surface of $Bi_{1-x}Sb_x$ NCs. More interestingly, the $Te^{2-}$-capped $Bi_{0.83}Sb_{0.17}$ NC based pellets (pellet **V**) showed a significantly higher $\sigma$ ($1.03 \times 10^5$ S/m) compared to the as-pressed pellets (pellet **I** and **II**) and even to the annealed pellet (pellet **III**), despite their relatively small grain size of ~15 nm. This high $\sigma$ of pellet **V** suggests efficient doping from $Te^{2-}$ ligands.[43]

**Temperature-Dependent Hall Measurements.** Electrical conductivity is determined by the product of the concentration ($n$) and mobility ($\mu$) of charge carriers: $\sigma = en\mu$ for unipolar transport. Both these parameters can show complex dependence of temperature and chemical factors. To obtain further insight into the charge transport in $Bi_{0.83}Sb_{0.17}$ NC based pellets, temperature-dependent $\mu$ and $n$ were obtained *via* the Hall measurements. The sign of the Hall coefficient ($R_H$) was negative throughout the whole temperature range for all pellets, indicating the n-type conductivity in $Bi_{0.83}Sb_{0.17}$ NCs with electrons as the majority carriers. The $\mu$ of the pellets was in the range $10^2$–$10^3$ $cm^2/(V\cdot s)$ at 300 K and gradually increased at low temperatures (Figure 5B). For comparison, reported room-temperature mobility for bulk $Bi_{1-x}Sb_x$ alloys is ~$10^3$ $cm^2/(V\cdot s)$.[44] On the other hand, the $n$ for the NC based pellets (Figure 5C) was higher compared to that of bulk $Bi_{1-x}Sb_x$ alloys probably due to the doping effect arising from defects and dangling bonds at the grain boundaries.

**TABLE 2. Carrier Mobility ($\mu$) and Average Grain Size (d) in Various $Bi_{0.83}Sb_{0.17}$ NC Based Pellets at 300 K**

| pellet | description | $\mu$ ($cm^2/(V\cdot s)$) | grain size, d (nm) |
|---|---|---|---|
| I | as-pressed, OLA | 82 | 15 |
| II | as-pressed, $N_2H_4$ | 118 | 18 |
| III | 250 °C annealed, OLA | 418 | 33 |
| IV | 250 °C annealed, $N_2H_4$ | 470 | 38 |
| V | as-pressed, $Te^{2-}$ | 112 | 15 |

Mobility data can be grouped in two families: all as-pressed NC pellets showed $\mu \approx 100 \pm 20$ $cm^2/(V\cdot s)$ at 300 K for the NCs capped with OLA (**I**), $N_2H_4$ (**II**), and $Te^{2-}$ (**V**) ligands. The samples annealed at 250 °C showed at room-temperature $\mu \approx 445 \pm 25$ $cm^2/(V\cdot s)$, again for the NCs capped with OLA (**III**) and $N_2H_4$ (**IV**) (Table 2). The mobility improvement upon annealing can be explained by the reduced number of grain boundaries which are well-known scattering sources of charge carriers. On the other hand, a moderate increase in both the $\mu$ and the grain size was observed after $N_2H_4$ treatment due to the removal of organic residue (from 82 to 118 $cm^2/(V\cdot s)$ for as-pressed pellets (**I** and **II**) and from 418 to 470 $cm^2/(V\cdot s)$ for 250 °C annealed pellets (**III** and **IV**)).

Experimental data suggest that $\mu$ values in the $Bi_{0.83}Sb_{0.17}$ NC based pellets are primarily governed by the average grain size ($d$) rather than by surface chemistry (Table 2). As shown in Figure S10, $\mu$ was roughly proportional to the average grain size ($d$), especially at low temperatures. In general, insensitivity of carrier mobility to interfacial chemistry is very uncommon in nanocrystalline materials. For example, carrier mobility in semiconductor NCs changes by many orders of magnitude when hydrocarbon ligands such as OLA are replaced by $N_2H_4$[28] and/or other small ligands.[23,24,27,30,46] Similarly, very strong dependence of conductivity on surface ligands was observed for arrays of metallic (Au) NCs.[47] In the case of $Bi_{0.83}Sb_{0.17}$, we observed a negative temperature coefficient for mobility ($d\mu/dT < 0$), characteristic of band-like transport. In combination with high overall mobility, which is probably higher than that in any previously reported NC-derived material, this suggests that the carrier mean free path (for bulk Bi, ~100 nm at 300 K and 400 $\mu$m at 4 K[45]) can exceed the size of individual grains, making mobility less sensitive to surface chemistry.

Similar to $\mu$, $n$ was also found to be considerably influenced by the grain size (Figure 5C and Table S3). Pellets **III** and **IV**, with grain sizes of ~35–40 nm, showed a significantly lower $n$ in comparison with pellets **I** and **II**, with grain sizes of 15–20 nm. The ~3-fold decrease in $n$ can be attributed to the reduction of the number of grain boundaries and thereby

the number of defects. Pellet **V** with $Te^{2-}$ showed the highest $n$ probably due to the existence of Te dopants, as well as a similar mobility to pellet **II**, indicating the efficient charge transport between NCs through the short $Te^{2-}$ ligands.

Compared to bulk polycrystalline $Bi_{1-x}Sb_x$ alloys, one distinguished feature of $Bi_{1-x}Sb_x$ NC based pellets with grain sizes from ~10 to ~40 nm is the weaker temperature dependence of both $\mu$ and $n$. In detail, the change of $\mu$ from 300 to 10 K was within 2−3-fold for all samples, while those for bulk alloys were reported to be as large as 2−3 orders of magnitude.[44] In particular, the as-pressed samples showed a much weaker temperature dependence of $\mu$ than annealed samples (Figure 5B), which might contribute to the very weak temperature dependence of $\sigma$. This could be explained if we take into account the process of carrier scattering, which can be qualitatively described by the empirical Matthiessen's rule, eq 1.[48]

$$\frac{1}{\mu_{tol}(T)} = \frac{1}{\mu_{bulk}(T)} + \frac{1}{\mu_{bound}(d)} + \frac{1}{\mu_{imp}(T)} \quad (1)$$

$$\mu \approx \mu_{bound}(d) \approx \mu^0 d \quad (2)$$

$$\sigma = en\mu \approx e(n_{int}(T) + n_D(T))\mu_{bound}(d) \quad (3)$$

Assuming each scattering mechanism is independent, the total scattering can be expressed as the sum of the contributions from different electron scattering processes: $\mu_{bulk}$ is the mobility determined solely by the scattering on acoustic phonons (dominant scattering process in bulk), $\mu_{bound}$ is the scattering at the interfaces and grain boundaries, $\mu_{imp}$ is the scattering by impurities, *etc*. eq 1.[12] Unlike the strong temperature dependence of the carrier scattering by acoustic phonons, the scattering at interfaces and impurities is mostly temperature independent.[12] Considering the small grain size (<40 nm) and thereby abundant grain boundaries in the NC-based pellets compared to bulk polycrystalline $Bi_{1-x}Sb_x$ alloys, we suggest that weak temperature dependence of $\mu$ below 140−160 K results from the reduced occupancy of acoustic phonons, leading to larger $\mu_{bulk}$, such that temperature-independent $\mu_{imp}$ and $\mu_{bound}$ prevail in $\mu_{tot}$. A similar weak temperature dependence of $\mu$ was observed in 65 nm $Bi_{1-x}Sb_x$ nanowire arrays embedded in anodic alumina templates.[13] Since the electron mean free path is much longer than $d$, $\mu$ in the NC-based samples could be approximately proportional to $d$ (eq 2, where $\mu^0$ is a constant), which is reasonable especially at low temperatures (Figure S10). Similarly, $n$ of the NC-based pellets also showed a weak temperature dependence, especially at low temperature (Figure 5C).

One of the most striking and counterintuitive trends observed in conductivity of our $Bi_{1-x}Sb_x$ NC based pellets is the convergence of $\sigma$ for annealed and as-pressed samples below ~140−160 K (Figure 5A). Samples **I** and **III** have the same initial surface chemistry, but the average grain size in sample **III** is significantly larger than in sample **I**, as well as mobility. The same applies to the pair of samples **II** and **IV**. The fact that both sample pairs show exactly the same conductivity below ~140−160 K suggests that mobility and free carrier concentration are inversely related to each other. Such behavior could be explained if we assume that all donors situate at the interfacial grain boundaries. In that case, the concentration of ionized dopants ($n_D$) is proportional to the total area of all grain boundaries per unit volume, which is inversely proportional to the grain size ($n_D \sim d^{-1}$). The free carrier concentration $n$ in the sample can be expressed as eq 4, where $n_{int}$ is the intrinsic carrier concentration, both $n^0$ and $n_D{}^0$ are constants, $\Delta E_g$ is the transport band gap, $\Delta E_D$ is the activation energy for the donor level, and $k$ is the Boltzmann constant.

$$n = n_{int} + n_D \approx n^0 \exp(-\Delta E_g/kT) + \frac{n_D{}^0}{d}\exp(-\Delta E_D/kT) \quad (4)$$

The biexponential fits of $n$ *vs* $T^{-1}$ for samples **I**−**IV** revealed $\Delta E_g$ =85 ± 5 meV, while $\Delta E_D$ was very small, less than 1 meV (Figure S11 and Table S4). The obtained $\Delta E_g$ value is somewhat larger than the bulk band gap, which could be a result of multiple factors, including quantum confinement and a Coulomb charging energy for nanograins.[49] In this case, we can neglect $n_{int}$ below 140 K and obtain $n \approx n_D{}^0/d$. By using this expression and eq 3, we obtain the conductivity independent of the grain size (eq 5) if grain chemistry does not change upon annealing. On the contrary, the contribution from the intrinsic carriers introduces the dependence in grain size at temperatures above ~140−160 K, and thus the annealed samples showed higher $\sigma$ than the as-pressed ones.

$$\sigma = en\mu \approx e\frac{n_D{}^0}{d}\mu^0 d \approx en_D{}^0\mu^0 \quad (5)$$

$Bi_{1-x}Sb_x$ NC based pellets with an average grain size ~10−40 nm show reasonable electrical conductivities and carrier mobilities compared to the bulk alloys. Furthermore, tuning grain sizes and surface chemistry (*e.g.*, *via* surfactant removal or doping) could independently control mobility and carrier concentration of $Bi_{1-x}Sb_x$-based nanostructured materials, suggesting opportunities for thermoelectric applications.

**Preliminary Evaluation of Thermoelectric Performance.** Semiconducting $Bi_{1-x}Sb_x$ alloys are considered as the state-of-the-art n-type thermoelectric material for use at very low temperatures (20−200 K). A theoretical study by Dresselhaus *et al.*[14] predicted anomalously high thermoelectric efficiency in $Bi_{1-x}Sb_x$ nanowires

**TABLE 3. Thermoelectric Properties of Various $Bi_{0.83}Sb_{0.17}$ NC Based Pellets at Room Temperature (300 K)**

| pellet | description | $\sigma$ ($10^5$ S/m) | $S$ ($\mu$V/K) | $\kappa$ (W/(m K)) | ZT |
|---|---|---|---|---|---|
| I | as-pressed, OLA | 0.68 ± 0.04 | −42 ± 2 | 1.37 ± 0.18 | 0.03 |
| II | as-pressed, $N_2H_4$ | 0.87 ± 0.05 | −63 ± 3 | 1.66 ± 0.22 | 0.06 |
| III | 250 °C annealed, OLA | 0.93 ± 0.05 | −78 ± 4 | 1.30 ± 0.17 | 0.13 |
| IV | 250 °C annealed, $N_2H_4$ | 1.11 ± 0.06 | −105 ± 6 | 1.63 ± 0.21 | 0.23 |

with diameter <∼40 nm at low temperatures. Furthermore, the controlled formation of grain boundaries may induce the carrier filtering effect[50] and therefore enhance the Seebeck coefficient by efficiently filtering the lower energy electrons. However, to the best of our knowledge, due to the difficulty in obtaining high-quality $Bi_{1-x}Sb_x$ nanostructures, there were only a few experimental reports on the thermoelectric performance of $Bi_{1-x}Sb_x$ nanowires and thin films.[10,13,51]

We conducted the characterization of the thermoelectric properties on our four $Bi_{1-x}Sb_x$ samples (**I**, **II**, **III**, and **IV**) with various grain sizes at room temperature (300 K) (Table 3). All samples exhibited negative Seebeck coefficient, $S$, in agreement with the negative Hall coefficient ($R_H$), which indicates n-type transport. The highest absolute value of $S$ was achieved for the sample **IV** ($S \approx -105$ $\mu$V/K), which was slightly higher than the average of those for the bulk $Bi_{1-x}Sb_x$ alloys (−80−90 $\mu$V/K).[4,5,17−19] The high $S$ might be attributed to the carrier filtering effect arising from the scattering at the potential barriers at the interfaces, as discussed in ref 19. Thermal conductivities ($\kappa$) of $Bi_{0.83}Sb_{0.17}$ NC based pellets were measured by the steady-state technique under high vacuum. $\kappa$ of these pellets was found to be in the range 1.3−1.6 W/(m K), which is substantially reduced compared to the reported values of bulk $Bi_{1-x}Sb_x$ alloys (4−6 W/(m K$^2$)).[5,19] The reduction in $\kappa$ can be attributed to the scattering of low-frequency phonons at the interfaces in the pressed NCs, as depicted in other nanostructured systems.[52,53]

The room-temperature $ZT$ for various $Bi_{0.83}Sb_{0.17}$ NC based pellets was calculated using $\sigma$, $S$, and $\kappa$. The highest $ZT$ (∼0.23) was achieved in pellet **IV**, which was comparable to single-crystal $Bi_{1-x}Sb_x$ and polycrystalline $Bi_{1-x}Sb_x$ (∼0.30). Considering the potential carrier filtering effect due to the carrier scattering at the nanostructured interfaces as well as the small grain size, the $Bi_{1-x}Sb_x$ NC based pellets are expected to exhibit promising thermoelectric performances at lower temperatures. Furthermore, better control of composition, doping, and grain sizes may enhance the thermoelectric performance, and this is our ongoing next step.

## CONCLUSIONS

In conclusion, we report the first colloidal synthesis of monodisperse, sub-10 nm $Bi_{1-x}Sb_x$ NCs. The reductive reaction pathway, used in this work, enabled good control over both the size and composition of NCs, despite the apparent difference in chemical reactivity of starting molecular Bi and Sb precursors. We expect that such an approach can be of general utility for the synthesis of alloy nanomaterials. The developed synthesis allowed us to explore the transport properties of $Bi_{1-x}Sb_x$ nanostructures with grain sizes in the range ∼10 to ∼40 nm for the first time. We also demonstrated the feasibility of tuning surface chemistry on the NCs with inorganic ligands, which can influence their transport properties by introducing doping effects. The $Bi_{1-x}Sb_x$ NC based pellets showed reasonably high electrical conductivity and carrier mobility, which are highly dependent on the grain size and surface chemistry. Unlike the bulk $Bi_{1-x}Sb_x$ alloys, the scattering at the grain boundaries dominated the carrier scattering process in the NC-based pellets, which led to a relatively weak temperature dependence of electron mobility. A room-temperature ZT of ∼0.23, comparable to that of bulk alloy, was obtained in the $Bi_{0.83}Sb_{0.17}$ NC based pellets without systematic optimizations.

## EXPERIMENTAL SECTION

**Synthesis of $Bi_{1-x}Sb_x$ NCs.** All syntheses and purifications of $Bi_{1-x}Sb_x$ NCs were based on conventional air-free techniques using a Schlenk line and a nitrogen-filled glovebox. In a typical synthesis of ∼9 nm $Bi_{0.84}Sb_{0.16}$ NCs, oleylamine (10 mL) was loaded into a three-necked flask and dried under vacuum at 100 °C for 1 h. In a glovebox, a precursor solution containing bismuth tris[bis(trimethylsilyl)amide] ($Bi[N(SiMe_3)_2]_3$, 0.2 mmol), tris(dimethylamido)antimony(III) ($Sb(NMe_2)_3$, 0.05 mmol), and lithium bis(trimethylsilyl)amide ($Li[N(SiMe_3)_2]$, 1.25 mmol) was prepared in 2 mL of anhydrous toluene. Then 1.25 mL of 1.0 M $LiEt_3BH$ in THF was injected into the reaction flask at 70 °C under $N_2$. After ∼15 s, the precursor solution in toluene was swiftly injected, resulting in the instant nucleation of $Bi_{1-x}Sb_x$ NCs, as indicated by the black color of the solution. After 15 s, the reaction mixture was rapidly cooled to room temperature. The crude solution was diluted by anhydrous toluene (v/v = 1:1) for the following washing process and centrifuged to separate the insoluble part from the stable colloidal solution. The NCs were isolated by adding acetonitrile (30−50% in volume of NC solution) and redissolved in common nonpolar solvents such as toluene or hexane.

To control the size and Sb content of $Bi_{1-x}Sb_x$ NCs, we tuned reaction parameters such as injection temperature, reaction time, and the ratio between $Bi[N(SiMe_3)_2]_3$ and $Sb(NMe_2)_3$. The ratio between the amount of $Li[N(SiMe_3)_2]$ (in moles) and the combined amount of Bi and Sb precursors (in moles) was kept at ∼5 for all the experiments. The ratio between $LiEt_3BH$ and the combined amount of Bi and Sb precursors was also kept at around 5.

**Synthesis of Inorganic Ligands.** MCC ligands ($K_4SnTe_4$, $(N_2H_5)_4Sn_2Se_6$, $(N_2H_5)_4Sn_2S_6$) were synthesized as described in refs 24, 54, and 55. Chalcogenide ligands ($Na_2S$, $Na_2Se$, $Na_2Te$) were synthesized according to ref 56. Additional details are provided in the Supporting Information.

**Exchange of Organic Ligands on $Bi_{1-x}Sb_x$ NCs with MCC and Metal-Free Ligands.** All ligand exchange procedures were carried out in a nitrogen-filled glovebox using anhydrous solvents. In a typical

ligand exchange using $K_4SnTe_4$, 1.5 mL of $Bi_{1-x}Sb_x$ NC solution in hexane (~2 mg/mL) was mixed with 2 mL of $K_4SnTe_4$ in DMSO (~5 mg/mL) and stirred or vigorously shaken for several minutes. Thereafter, $Bi_{1-x}Sb_x$ NCs completely transferred to the bottom phase (DMSO) and formed a dark brown solution. The DMSO phase was separated out, followed by a triple wash with hexane to remove any residual organic ligands. The $Bi_{1-x}Sb_x$ NCs were precipitated out with 1−2 mL of acetonitrile. The precipitates can redisperse in polar solvents such as DMSO, hydrazine ($N_2H_4$), formamide, and *N*-methylformamide at a concentration of at least 5 mg/mL.

Ligand exchange with metal-free ligands ($S^{2-}$, $Se^{2-}$, $Te^{2-}$) was carried out in a similar way, except saturated ligand solution in DMSO was adopted as the polar phase.

**Surfactant Removal by $N_2H_4$ Treatment and Preparation of $Bi_{1-x}Sb_x$ NC Pellets.** $Bi_{1-x}Sb_x$ NCs in toluene were precipitated by the addition of acetonitrile (v/v = 1:3). The powdery form of $Bi_{1-x}Sb_x$ NCs was retrieved by centrifugation, and the powder was washed several times with acetonitrile and ethanol. For a complete removal of organic surfactants in the $Bi_{1-x}Sb_x$ NC powder, $N_2H_4$ treatment was carried out under an inert atmosphere. In detail, $Bi_{1-x}Sb_x$ NC powder (~1.0 g) was dispersed in a $N_2H_4$ solution (10 mL, 1.0 M in acetonitrile) and sonicated or stirred for 10−15 min. NC powder was separated by decanting the supernatant and treated by $N_2H_4$ solution another two times. Afterward, the $Bi_{1-x}Sb_x$ NC powder was washed by ethanol to remove $N_2H_4$ and retrieved by centrifugation. Finally, the powder was dried under vacuum overnight to remove residual solvents.

To prepare $Bi_{1-x}Sb_x$ NC based pellets, dried $Bi_{1-x}Sb_x$ NC powder with or without surfactant removal (*i.e.*, $N_2H_4$ treatment) was pressed in a stainless steel die into square (6 mm side, thickness ~1−2 mm) or round disk (6 or 13 mm in diameter, thickness ~1−2 mm)-shaped pellets under ~15 MPa for 30 min at room temperature. For the $Te^{2-}$-capped $Bi_{1-x}Sb_x$ NC based pellet, NCs in DMSO were precipitated out by the addition of acetonitrile and dried under vacuum. The dried powder of $Te^{2-}$-capped $Bi_{1-x}Sb_x$ NCs was then pressed into a pellet. The heat treatment on the NC-based pellets was performed in an oven in a nitrogen-filled glovebox.

**Characterization Techniques.** TEM images were obtained using a 300 kV FEI Tecnai F30 microscope. Wide angle powder X-ray diffraction patterns were measured using a Bruker D8 diffractometer with a Cu Kα X-ray source operating at 40 kV and 40 mA. The average grain size in $Bi_{1-x}Sb_x$ NC based pellets was estimated by Scherrer's equation. The instrumental broadening was deconvoluted from the Scherrer broadening with the method described in ref 57. Inductively coupled plasma optical emission spectroscopy analysis was carried out on an Agilent 700 Series to determine Sb content in $Bi_{1-x}Sb_x$ NCs. Fourier transform infrared spectra were acquired with a Nicole Nexus-670 FTIR spectrometer. Samples for FTIR measurements were prepared by drop casting NC dispersions on a KBr substrate for the solution sample or pressing a pellet with KBr powder for the powdery form sample, respectively. Differential scanning calorimetry data were obtained using a Shimadzu TGA-50 thermal analyzer at a heating rate of 5 °C/min under a nitrogen flow. Zeta-potential data were collected using a Zetasizer Nano-ZS (Malvern Instruments, UK).

**Charge Transport and Thermoelectric Properties of $Bi_{1-x}Sb_x$ NC Based Pellets.** All the charge transport measurements were carried out under an inert atmosphere. Temperature-dependent electrical conductivity and Hall measurements of $Bi_{1-x}Sb_x$ NC based pellets were conducted in a physical property measurement system (PPMS, Quantum Design) under a helium atmosphere in the temperature range 10−300 K. The electrical conductivity and Hall coefficient were measured using a van der Pauw configuration, where four isolated gold wires were glued (by conductive silver paste) at the corners of the pellets. For Hall measurement, a magnetic field of 1.0 T together with a direct current of 0.1 A was applied. Under this magnetic field, the magnetoresistance (MR = $(R - R_o)/R$, where $R$ and $R_o$ are the resistance with and without applied magnetic field, respectively) was within 3%. The measurements were controlled by a Keithley multimeter (Keithley 2400) through a Labview interface. Seebeck coefficients (*S*, also known as the thermopower) of pellets on perpendicular and horizontal directions were measured at 300 K by a homemade setup and commercial Seebeck effect measurement system (MMR Technologies, Inc.), respectively. *S* values measured in both directions were within the range of ±5%, revealing the isotropic properties originated from the randomly oriented grains. Thermal conductivity measurements were carried out using a homemade setup for steady-state thermal conductivity measurements under high vacuum, as described in the Supporting Information.

*Conflict of Interest:* The authors declare no competing financial interest.

*Supporting Information Available:* Additional experimental details, figures, and tables. This material is available free of charge *via* the Internet at http://pubs.acs.org.

*Acknowledgment.* We thank W. Liu and M. Boles for the discussion on the synthesis of $Bi_{1-x}Sb_x$ NCs and D. Dolzhnikov for the synthesis of metal-free chalcogenide ligands. This work was supported by the II-VI Foundation and the NSF MRSEC Program under Award Number DMR-0213745. J.A.M. and W-L.O. acknowledge support from the AFOSR Young Investigator Program (FA95501110030) and the NSF CAREER Award (ENG-1149374).

## REFERENCES AND NOTES

1. Lenoir, B.; Cassart, M.; Michenaud, J.-P.; Scherrer, H.; Scherrer, S. Transport Properties of Bi-Rich Bi-Sb Alloys. *J. Phys. Chem. Solids* **1996**, *57*, 89–99.
2. Banerjee, A.; Fauque, B.; Izawa, K.; Miyake, A.; Sheikin, I.; Flouquet, J.; Lenoir, B.; Behnia, K. Transport Anomalies across the Quantum Limit in Semimetallic $Bi_{96}Sb_4$. *Phys. Rev. B* **2008**, *78*, 161103.
3. Smith, G. E.; Wolfe, R. Thermoelectric Properties of Bismuth-Antimony Alloys. *J. Appl. Phys.* **1962**, *33*, 841–846.
4. Yim, W. M.; Amith, A. Bi-Sb Alloys for Magneto-Thermoelectric and Thermomagnetic Cooling. *Solid-State Electron.* **1972**, *15*, 1141–1165.
5. Lenoir, B.; Dauscher, A.; Cassart, M.; Ravich, Y. I.; Scherrer, H. Effect of Antimony Content on the Thermoelectric Figure of Merit of $Bi_{1-x}Sb_x$ Alloys. *J. Phys. Chem. Solids* **1998**, *59*, 129–134.
6. Fu, L.; Kane, C. L. Topological Insulators with Inversion Symmetry. *Phys. Rev. B* **2007**, *76*, 045302.
7. Hsieh, D.; Qian, D.; Wray, L.; Xia, Y.; Hor, Y. S.; Cava, R. J.; Hasan, M. Z. A Topological Dirac Insulator in a Quantum Spin Hall Phase. *Nature* **2008**, *452*, 970–974.
8. Smith, G. E. Experimental Determination of Effective Masses in a Bismuth-Antimony Alloy. *Phys. Rev. Lett.* **1962**, *9*, 487–489.
9. Oelgart, G.; Herrmann, R. Cyclotron Resonance and Quantum Oscillations of p-Type Semiconducting $Bi_{1-x}Sb_x$ Alloys. *Phys. Status Solidi B* **1974**, *61*, 137–146.
10. Lin, Y.-M.; Cronin, S.; Rabin, O.; Ying, J. Y.; Dresselhaus, M. S. Transport Properties of $Bi_{1-x}Sb_x$ Alloy Nanowires Synthesized by Pressure Injection. *Appl. Phys. Lett.* **2001**, *79*, 677–679.
11. Roh, J. W.; Hippalgaonkar, K.; Ham, J. H.; Chen, R.; Li, M. Z.; Ercius, P.; Majumdar, A.; Kim, W. C.; Lee, W. Y. Observation of Anisotropy in Thermal Conductivity of Individual Single-Crystalline Bismuth Nanowires. *ACS Nano* **2011**, *5*, 3954–3960.
12. Lin, Y.-M.; Cronin, S. B.; Ying, J. Y.; Dresselhaus, M. S.; Heremans, J. P. Transport Properties of Bi Nanowire Arrays. *Appl. Phys. Lett.* **2000**, *76*, 3944–3946.
13. Lin, Y.-M.; Rabin, O.; Cronin, S.; Ying, J. Y.; Dresselhaus, M. S. Semimetal-Semiconductor Transition in $Bi_{1-x}Sb_x$ Alloy Nanowires and Their Thermoelectric Properties. *Appl. Phys. Lett.* **2002**, *81*, 2403–2405.
14. Rabin, O.; Lin, Y.-M.; Dresselhaus, M. S. Anomalously High Thermoelectric Figure of Merit in $Bi_{1-x}Sb_x$ Nanowires by Carrier Pocket Alignment. *Appl. Phys. Lett.* **2001**, *79*, 81–83.

15. Dutta, S.; Shubha, V.; Ramesh, T. G.; D'Sa, D. Thermal and Electronic Properties of $Bi_{1-x}Sb_x$ Alloys. *J. Alloys Compd.* **2009**, *467*, 305–309.
16. Devaux, X.; Brochin, F.; Martin-Lopez, R.; Scheele, H. Study of the Microstructure Influence on the Transport Properties of $Bi_{86.5}Sb_{13.5}$ Polycrystalline Alloy. *J. Phys. Chem. Solids* **2002**, *63*, 119–125.
17. Heinz, N. A.; Howell, S.; Wang, H.; Ikeda, T.; Snyder, G. J. Hot Pressing and Nanostructuring of $Bi_{90}Sb_{10}$ Alloys to Concurrently Improve Mechanical and Thermoelectric Properties. *Phys. Status Solidi A* **2012**, *209*, 2565–2569.
18. Lukas, K. C.; Joshi, G.; Modic, K.; Ren, Z. F.; Opeil, C. P. Thermoelectric Properties of Ho-Doped $Bi_{0.88}Sb_{0.12}$. *J. Mater. Sci.* **2012**, *47*, 5729–5734.
19. Martin-Lopez, R.; Dauscher, A.; Scherrer, H.; Hejtmanek, J.; Kenzari, H.; Lenoir, B. Thermoelectric Properties of Mechanically Alloyed Bi-Sb Alloys. *Appl. Phys. A: Mater. Sci. Process.* **1999**, *68*, 597–602.
20. Datta, A.; Nolas, G. S. Composition Controlled Synthesis of Bi Rich $Bi_{1-x}Sb_x$ Alloy Nanocrystals by a Low Temperature Polyol Process. *CrystEngComm* **2011**, *13*, 2753–2757.
21. Sumithra, S.; Misra, D. K.; Wei, C.; Gabrisch, H.; Poudeu, P. F. P.; Stokes, K. L. Solvothermal Synthesis and Analysis of $Bi_{1-x}Sb_x$ Nanoparticles. *Mater. Sci. Eng., B* **2011**, *176*, 246–251.
22. Zhou, B.; Zhu, J.-J. A Chemical Solution Route to Rapid Synthesis of Homogeneous $Bi_{100-x}Sb_x$ Alloys Nanoparticles at Room Temperature. *J. Nanosci. Nanotechnol.* **2007**, *7*, 525–529.
23. Nag, A.; Kovalenko, M. V.; Lee, J.-S.; Liu, W. Y.; Spokoyny, B.; Talapin, D. V. Metal-Free Inorganic Ligands for Colloidal Nanocrystals: $S^{2-}$, $HS^-$, $Se^{2-}$, $HSe^-$, $Te^{2-}$, $HTe^-$, $TeS_3^{2-}$, $OH^-$, and $NH_2^-$ as Surface Ligands. *J. Am. Chem. Soc.* **2011**, *133*, 10612–10620.
24. Kovalenko, M. V.; Scheele, M.; Talapin, D. V. Colloidal Nanocrystals with Molecular Metal Chalcogenide Surface Ligands. *Science* **2009**, *324*, 1417–1420.
25. Kovalenko, M. V.; Bodnarchuk, M. I.; Zaumseil, J.; Lee, J.-S.; Talapin, D. V. Expanding the Chemical Versatility of Colloidal Nanocrystals Capped with Molecular Metal Chalcogenide Ligands. *J. Am. Chem. Soc.* **2010**, *132*, 10085–10092.
26. Kovalenko, M. V.; Spokoyny, B.; Lee, J.-S.; Scheele, M.; Weber, A.; Perera, S.; Landry, D.; Talapin, D. V. Semiconductor Nanocrysals Functionalized with Antimony Telluride Zintl Ions for Nanostructured Thermoelectrics. *J. Am. Chem. Soc.* **2010**, *132*, 6686–6695.
27. Nag, A.; Chung, D. S.; Dolzhnikow, D. S.; Dimitrijevic, N. M.; Chattopadhyay, S.; Shibata, T.; Talapin, D. V. Effect of Metal Ions on Photoluminescence, Charge Transport, Magnetic and Catalytic Properties of All-Inorganic Colloidal Nanocrystals and Nanocrystal Solids. *J. Am. Chem. Soc.* **2012**, *134*, 13604–13615.
28. Talapin, D. V.; Murray, C. B. PbSe Nanocrystal Solids for n- and p-Channel Thin Film Field-Effect Transistors. *Science* **2005**, *310*, 86–89.
29. Talapin, D. V.; Lee, J.-S.; Kovalenko, M. V.; Shevchenko, E. V. Prospects of Colloidal Nanocrystals for Electronic and Optoelectronic Applications. *Chem. Rev.* **2010**, *110*, 389–458.
30. Lee, J.-S.; Kovalenko, M. V.; Huang, J.; Chung, D. S.; Talapin, D. V. Band-Like Transport, High Electron Mobility and High Photoconductivity in All-Inorganic Nanocrystal Arrays. *Nat. Nanotechnol.* **2011**, *6*, 348–352.
31. Yarema, M.; Kovalenko, M. V.; Hesser, G.; Talapin, D. V.; Heiss, W. Highly Monodisperse Bismuth Nanoparticles and Their Three-Dimensional Superlattices. *J. Am. Chem. Soc.* **2010**, *132*, 15158–15159.
32. Wang, F.; Tang, R.; Yu, H.; Gibbons, P. C.; Buhro, W. E. Size- and Shape-Controlled Synthesis of Bismuth Nanoparticles. *Chem. Mater.* **2008**, *20*, 3656–3662.
33. Shin, J.; Verma, A.; Stringfellow, G. B.; Gedridge, R. W., Jr. Trisdimethylaminoantimony: A New Sb Source for Low Temperature Epitaxial Growth of InSb. *J. Cryst. Growth* **1994**, *143*, 15–21.
34. Shin, J.; Hsu, Y.; Hsu, T. C.; Stringfellow, G. B.; Gedridge, R. W., Jr. InSb, GaSb, and GaInSb Grown Using Trisdimethylamino Antimony. *J. Electron. Mater.* **1995**, *24*, 1563–1569.
35. Liu, W. Y.; Chang, A. Y.; Schaller, R. D.; Talapin, D. V. Colloidal InSb Nanocrystals. *J. Am. Chem. Soc.* **2012**, *134*, 20258–20261.
36. Richards, V. N.; Shields, S. P.; Buhro, W. E. Nucleation Control in the Aggregative Growth of Bismuth Nanocrystals. *Chem. Mater.* **2011**, *23*, 137–144.
37. Lenoir, B.; Demouge, A.; Perrin, D.; Scherrer, H.; Scherrer, S.; Cassart, M.; Michenaud, J.-P. Growth of BiSb Alloys by the Traveling Heater Method. *J. Phys. Chem. Solids* **1995**, *56*, 99–105.
38. Berger, H.; Christ, B.; Troschke, J. Lattice Parameter Study in the $Bi_{1-x}Sb_x$ Solid-Solution System. *Cryst. Res. Technol.* **1982**, *17*, 1233–1239.
39. Cucka, P.; Barrett, C. S. The Crystal Structure of Bi and of Solid Solutions of Pb, Sn, Sb and Te in Bi. *Acta Crystallogr.* **1962**, *15*, 865–872.
40. Martin-Lopez, R.; Lenoir, B.; Devaux, X.; Dauscher, A.; Scherrer, H. Mechanical Alloying of BiSb Semiconducting Alloys. *Mater. Sci. Eng., A* **1998**, *A248*, 147–152.
41. Olson, E. A.; Efremov, M. Y.; Zhang, M.; Zhang, Z.; Allen, L. H. Size Dependent Melting of Bi Nanoparticles. *J. Appl. Phys.* **2005**, *97*, 034304.
42. Ong, W.-L.; Rupich, S. M.; Talapin, D. V.; McGaughey, A. J. H.; Malen, J. A. Surface Chemistry Mediates Thermal Transport in Three-Dimensional Nanocrystals Arrays. *Nat. Mater.* **2013**, *12*, 410–415.
43. Cho, S.; DiVenere, A.; Wong, G. K.; Ketterson, J. B.; Meyer, J. R. Thermoelectric Transport Properties of N-Doped and P-Doped $Bi_{0.91}Sb_{0.09}$ Alloy Thin Films. *J. Appl. Phys.* **1999**, *85*, 3655–3660.
44. Kitagawa, H.; Noguchi, H.; Kiyabu, T.; Itoh, M.; Noda, Y. Thermoelectric Properties of BiSb Semiconducting Alloys Prepared by Quenching and Annealing. *J. Phys. Chem. Solids* **2004**, *65*, 1223–1227.
45. Heremans, J.; Thrush, C. M.; Lin, Y.-M.; Cronin, S.; Zhang, Z.; Dresselhaus, M. S.; Mansfield, J. F. Bismuth Nanowire Arrays: Synthesis and Galvanomagnetic Properties. *Phys. Rev. B* **2000**, *61*, 2921–2930.
46. Fafarman, A. T.; Koh, W. K.; Diroll, B. T.; Kim, D. K.; Ko, D. K.; Oh, S. J.; Ye, X.; Doan-Nguyen, V.; Crump, M. R.; Reifsnyder, D. C.; *et al*. Thiocyanate-Capped Nanocrystals Colloids: Vibration Reporter of Surface Chemistry and Solution-Based Route to Enhanced Coupling in Nanocrystal Solids. *J. Am. Chem. Soc.* **2011**, *133*, 15753–15761.
47. Zabet-Khosousi, A.; Dhirani, A.-A. Charge Transport in Nanoparticle Assemblies. *Chem. Rev.* **2008**, *108*, 4072–4124.
48. Ashcroft, N. W.; Mermin, N. D. *Solid State Physics*; Holt, Rinehart and Winston: New York, 1976.
49. Beloborodov, I. S.; Lopatin, A. V.; Vinokur, V. M.; Efetov, K. B. Granular Electronic Systems. *Rev. Mod. Phys.* **2007**, *79*, 469–518.
50. Heremans, J.; Thrush, C. M.; Morelli, D. T. Thermopower Enhancement in Lead Telluride Nanostructures. *Phys. Rev. B* **2004**, *70*, 115334.
51. Vurgaftman, I.; Meyer, J. R.; Hoffman, C. A.; Cho, S.; DiVenere, A.; Wong, G. K.; Ketterson, J. B. Thermoelectric and Magnetotransport Properties of $Bi_{1-x}Sb_x$ Thin Films and Bi/CdTe Superlattices. *J. Phys.: Condens. Matter* **1999**, *11*, 5157–5167.
52. Hsu, K. F.; Loo, S.; Guo, F.; Chen, W.; Dyck, J. S.; Uher, C.; Hogan, T. P.; Polychroniadis, E. K.; Kanatzidis, M. G. Cubic $AgPb_mSbTe_{2+m}$: Bulk Thermoelectric Materials with High Figure of Merit. *Science* **2004**, *303*, 808–821.
53. Poudel, B.; Hao, Q.; Ma, Y.; Lan, Y.; Minnich, A.; Yu, B.; Yan, X.; Wang, D.; Muto, A.; Vashaee, D.; *et al*. High-Temperature Performance of Nanostructured Bismuth Antimony Telluride Bulk Alloys. *Science* **2008**, *320*, 634–638.
54. Huffman, J. C.; Haushalter, J. P.; Umarji, A. M.; Shenoy, G. K.; Haushalter, R. C. Synthesis of Tin-Tellurium Polyanions: Structure of $(Me_4N)_4Sn_2Te_6$. *Inorg. Chem.* **1984**, *23*, 2312–2315.
55. Korlann, S. D.; Riley, A. E.; Kirsch, B. L.; Mun, B. S.; Tolbert, S. H. Chemical Tuning of the Electronic Properties in a

Periodic Surfactant-Templated Nanostructured Semiconductor. *J. Am. Chem. Soc.* **2005**, *127*, 12516–12527.
56. Shaw, G. A.; Parkin, I. P. Liquid Ammonia Mediated Metathesis: Synthesis of Binary Metal Chalcogenides and Pnictides. *Inorg. Chem.* **2001**, *40*, 6940–6947.
57. Jiang, C. Y.; Lee, J.-S.; Talapin, D. V. Soluble Precursors for $CuInSe_2$, $CuIn_{1-x}Ga_xSe_2$, and $Cu_2ZnSn(S,Se)_4$ Based on Colloidal Nanocrystals and Molecular Metal Chalcogenide Surface Ligands. *J. Am. Chem. Soc.* **2012**, *134*, 5010–5013.